Pharmaceutical Research, Vol. 8, No. 6, 1991

Review

Introduction to Fourier Transform Infrared Spectroscopy and Applications in the Pharmaceutical Sciences

Robert J. Markovich[1] and Charles Pidgeon[1,2]

The applications of infrared spectroscopy to pharmaceutical sciences is small compared to the applications of infrared spectroscopy to the fields of chemistry, biology, and biochemistry. This is unfortunate because modern routine infrared spectrometers are excellent research tools that provide very high signal-to-noise, high resolution, and extensive data-manipulation computer software packages. This review summarizes basic principles of infrared spectrometers and the use of Fourier self-deconvolution.

KEY WORDS: infrared (IR) spectroscopy; Fourier transform IR (FTIR); pharmaceutical applications.

INTRODUCTION

Infrared spectra of pharmaceutical systems frequently contain overlapping infrared (IR) bands that are *instrumentally unresolvable*. Overlapping IR bands are a particularly common problem in the infrared spectra of condensed phase samples because the widths of individual absorption bands are usually greater than the separation between neighboring bands. Unfortunately, increasing the instrumental resolution does not resolve overlapping bands, and consequently mathematical methods are needed to resolve complex band contours into their individual components. The mathematical techniques currently used to overcome spectral band overlap include curve-fitting (1), derivative spectroscopy (2), and Fourier deconvolution (3–10). Of these techniques, Fourier deconvolution provides the most information on band structure, especially when the individual component bandwidths are similar. Although Fourier deconvolution is a powerful technique common to infrared spectroscopy, a functional understanding of deconvolution theory must precede its use because artifacts such as water vapor band intensities (2,5) and background noise (4,8,9) are enhanced by Fourier deconvolution and these artifacts may be mistaken for real spectral features. Thus, understanding spectral deconvolution allows the user to make the correct choice of both the spectrometer parameters used to collect the IR data and the deconvolution parameters needed to resolve complex IR band contours into their individual components (2,3,5,6,9,10). With the correct choice of both the spectral and the deconvolution parameters, optimum resolution enhancement occurs.

Applications of infrared spectroscopy to the pharmaceutical sciences are rapidly expanding and these applications are briefly reviewed after describing how Fourier transform infrared spectrometers collect and process data.

[1] Department of Medicinal Chemistry, School of Pharmacy, Purdue University, West Lafayette, Indiana 47907.

[2] To whom correspondence should be addressed.

FOURIER TRANSFORM INFRARED SPECTROMETERS

Interferometers

Experimentally, Fourier transform infrared (FTIR) spectrometers measure interferograms with an optical device known as an interferometer, which is based upon the Michelson interferometer shown in Fig. 1 (11–14). This interferometer consists of two plane mirrors at right angles to each other and a beam splitter at a 45° angle to the mirrors. One mirror is fixed, while the other is movable. For mid-IR spectroscopy, the beam splitter is composed of a very thin film of germanium supported on a transmitting KBr substrate. The beam splitter divides the incoming light from the source into each arm of the interferometer, ideally reflecting 50% of the light to the moving mirror and transmitting 50% of the light to the fixed mirror. Thus as shown in Fig. 1, the input beam of light is equally divided into two optical paths of the interferometer; one arm of the interferometer has a fixed optical path length, while the other arm of the interferometer has a variable optical path length created by the movable mirror. However, the two reflected beams recombine at the beam splitter, and during this second pass through the beam splitter approximately half the beam returns to the source and the other half passes through the sample where the nonabsorbed light continues on to the detector. The optical path difference caused by the movable mirror results in a phase difference when the reflected light beams are recombined; this produces a time-dependent optical interference pattern at the detector. This optical interference pattern, encoding the spectral information about the sample, is called an interferogram. Thus, the major function of the interferometer is to divide the light from the IR source into two optical paths (one with a fixed optical path length and one

0724-8741/91/0600-0663$06.50/0

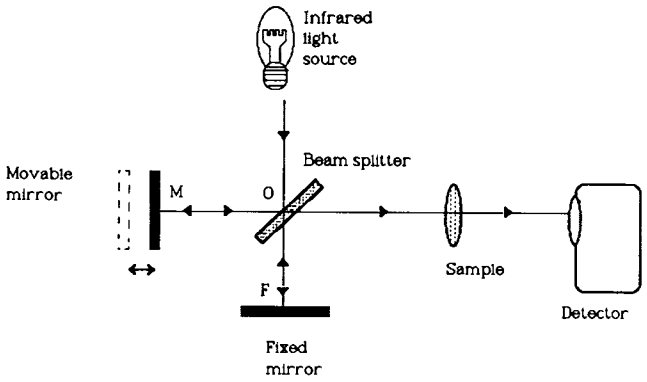

Fig. 1. Essential components of a Michelson interferometer. During an infrared scan, the interferometer sequentially (i) divides light emitted from the IR source in two beams using a beam splitter, (ii) changes the optical path of one beam using a movable mirror, (iii) recombines the two beams to create optical interference, and (iv) passes the IR light through the sample for measurement of a single-beam spectrum. The ratio of the single-beam spectra with and without the sample in the light path yields a sample spectrum in percentage transmittance. As shown, the moving mirror cycles back and forth during an FTIR scan. The *optical path difference* for any mirror displacement x is calculated by the equation $|2(OM - OF)|$ and is denoted *optical retardation* δ.

with a variable optical path length) and then recombine the two beams of light to create an optical interference pattern denoted as an interferogram. Interferograms are plots of the light intensity $I(\delta)$ from the IR source reaching the detector versus the optical retardation δ caused by the displacement of the mirror. The maximum light intensity reaching the detector is referred to as throughput and, in part, determines the instrument sensitivity.

Detectors

Both the detector and the IR crystal surface control the lower limit of the IR spectral window during data collection. Two types of detectors are used in modern infrared spectrometers: a deuterated triglycine sulfate (TGS) pyroelectric bolometer, which is the least expensive and supplied with the purchase of most spectrometers, and a more sensitive liquid nitrogen-cooled mercury cadmium telluride (MCT) photodetector. MCT detectors are preferred for IR measurements of condensed phase samples, particularly liquid phase, because MCT detectors are more sensitive than TGS detectors. Three different MCT detectors are available and each detector is defined by its lower limit wavenumber cutoff, $\bar{\nu}_{cutoff}$. The narrow-range MCT detector has a $\bar{\nu}_{cutoff}$ ~800 cm^{-1}, the medium-range MCT detector has a $\bar{\nu}_{cutoff}$ ~650 cm^{-1}, and the wide-range MCT detector has a $\bar{\nu}_{cutoff}$ ~500 cm^{-1}. Although the sensitivity of these MCT detectors varies with $\bar{\nu}_{cutoff}$, the narrow-range MCT detector elicits the highest sensitivity (10 times the sensitivity of the TGS detector) and the wide-range MCT detector has an intermediate sensitivity (three to four times the sensitivity of the TGS detector) (11,15).

The IR light intensity (or optical throughput) of the interference pattern reaching the detector is quantitated at intervals of mirror displacement, x, that are less than a micrometer. This optical throughput is quantitated at equal intervals of mirror displacement and therefore the interferogram sample spacing is fixed. FTIR spectrometers have a helium–neon (He–Ne) laser to measure the linear displacement of the movable mirror so that the computer can quantitate the optical throughput at exact mirror displacements in the form of digitized data. Consequently the He–Ne laser is sometimes referred to as the IR spectrometers' clock that tells the computer when to obtain a data point for the interferogram being measured. The He–Ne laser emits light with a wavelength of 0.63299 μ (compared to the wavelengths 2.5 through 25 μ defining the mid IR region) and the position of the moving mirror can be accurately evaluated at one-half of the laser wavelength but usually one wavelength is used as the spacing interval. Sophisticated (and expensive) FTIR spectrometers allow the user to define the sample spacing, but for most mid-IR work this is unnecessary.

Interferograms

Understanding how interferograms encode spectral information is conveniently described by first considering a monochromatic laser-light source entering a Michelson interferometer. When laser light enters an interferometer, only a single wavelength of light can exit the interferometer. However, at the detector, the laser light appears to alternate from light to dark at increments of mirror movement x, producing a maximum signal at mirror positions eliciting maximum constructive interference and a minimum signal at mirror positions eliciting maximum destructive interference. At mirror positions between the maximum constructive interference and the maximum destructive interference, optical interference causes the input laser light to appear at some intermediate intensity. Although the incident laser-light intensity is constant, the interferometer transformed the high-frequency IR beam into a modulated beam of varying intensity as the moving mirror travels through one cycle. Thus the output of the interferometer is merely a beam of light, oscillating in intensity. A plot of this oscillating beam intensity $I(x)$ versus mirror movement x [or, equivalently, $I(\delta)$ versus optical retardation δ] is shown in Fig. 2A. We note that the output of an interferometer actually contains both an AC and a DC component. The DC component is omitted for clarity

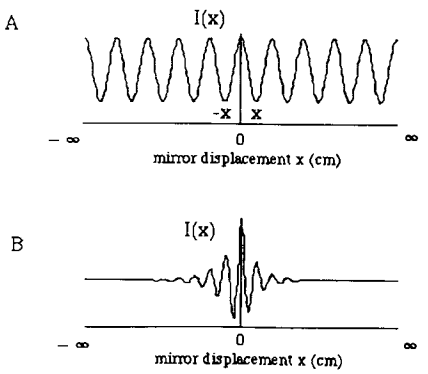

Fig. 2. Output from a Michelson interferometer as a function of mirror displacement x. The interferograms $I(x)$ are for a monochromatic IR source (A) and a polychromatic IR source (B). Both interferograms are even functions, $I(-x) = I(x)$.

because the spectral information is encoded in the AC component.

Figure 2A shows that the interferogram of a laser-light source is a pure cosine wave with a constant amplitude. This can be explained by considering the detector signal at discrete mirror positions. The optical path difference between the light beams which recombine at the beam splitter is calculated by the equation $|2(OM - OF)|$ and is referred to as optical retardation δ. Starting from the point where the fixed and moving mirrors have a zero path difference ZPD (i.e., OM = OF as shown in Fig. 1), the two beams interfere constructively and the detector observes a maximum signal intensity. As shown in Fig. 2, this mirror position is at the center of the interferogram. If the movable mirror is displaced a distance 1/4 λ away from this ZPD, the optical retardation is now 1/2 λ. The laser beams in each arm of the interferometer are exactly 180° out of phase, and upon recombination at the beam splitter, destructive interference causes a minimum detector response. A further displacement of 1/4 λ makes the total optical retardation λ, and the two beams are once more in phase and the condition of constructive interference exists. Therefore for a monochromatic IR beam, there is no way to determine whether the signal maximum corresponds to ZPD or some integral number of λ.

Actually modern FTIR spectrometers do not stop the mirror at individual positions of mirror displacement as described above; rather the mirror moves at a constant velocity during a scan. Consequently the signal intensity $I(\delta)$ oscillates during each 1/2 λ of optical retardation δ. In theory, the interferogram of a monochromatic source is a simple cosine function described by (11)

$$I(\delta) = 0.5\, I(\bar{\nu}) \cos\left(2\pi \frac{\delta}{\lambda}\right) \tag{1a}$$

$$= 0.5\, I(\bar{\nu}) \cos(2\pi\bar{\nu}\delta) \tag{1b}$$

where $I(\bar{\nu})$ is the IR source intensity, δ is the optical path difference $|2(OM - OF)|$, λ is the wavelength of light, and $1/\lambda = \bar{\nu}$. The factor 0.5 in Eq. (1) results from a physical limitation of the interferometer; due to the position of the optical components in the interferometer, only 50% of the reflected light that recombines at the beam splitter travels toward the detector, whereas 50% returns toward the source. Even for this trivial case using a monochromatic IR source, the experimentally recorded interferogram is actually a function of several instrument variables which include the intensity of the light source, beam-splitter efficiency, detector response, and amplifier characteristics (11). Because each of these *instrument* variables affects the optical throughput of $I(\bar{\nu})$ measured at the detector, Eq. (1) must be rewritten as

$$I(\delta) = B(\bar{\nu}) \cos(2\pi\nu\delta) \tag{2}$$

where $B(\bar{\nu})$ is the intensity from the IR light source emitted at a specific wavenumber $\bar{\nu}$ as modified by the instrument (11). The optical retardation t seconds after ZPD is given by

$$\delta = 2Vt \tag{3}$$

where V is the velocity of the movable mirror in centimeters per second (11). During a scan, the product Vt [in Eq. (3)] is the distance of mirror movement x (i.e., $x = Vt$), and since the reflected light from the moving mirror travels twice the distance that the mirror has moved, the factor 2 in Eq. (3) is needed. In other words, optical retardation δ is always twice the distance of mirror movement (i.e., $\delta = 2x$). Substituting Eq. (3) into the argument of the cosine function in Eq. (2) gives

$$I(t) = B(\bar{\nu}) \cos(2\pi\bar{\nu}\, 2Vt) \tag{4}$$

Equations (2) and (4) are mathematically equivalent. However, the "new" dependent variable $I(t)$ is the optical throughput at the detector as a function of the new independent variable time t. Equation (4) is a cosine wave and the amplitude at time t of any cosine wave of frequency f can be described by the general equation

$$A(t) = A_0 \cos(2\pi f t) \tag{5}$$

where A_0 is the maximum amplitude of the wave (11). Equation (4) is identical to Eq. (5), where

$$A(t) = I(\mathrm{t}) \tag{6a}$$

$$A_0 = B(\bar{\nu}) \tag{6b}$$

$$f = 2V\bar{\nu} \tag{6c}$$

Thus the interferogram intensity $I(x)$ [or $I(t)$] resulting from laser light entering an interferometer, as shown in Fig. 2A, is a pure cosine wave with a frequency f and maximum amplitude $B(\bar{\nu})$. A real infrared source emits broadband IR radiation, thus each $\bar{\nu}$ emitted contributes a pure cosine wave to the final interferogram and the amplitude of each cosine wave in the experimentally measured interferogram depends in part on the intensity of the particular $\bar{\nu}$ emitted from the IR source. In fact, based on Eq. (6c), each unique $\bar{\nu}$ emitted from any IR source is transformed by the interferometer into a unique cosine-wave interferogram whose modulation frequency f is dependent on the mirror velocity V.

Equation (6c) is a mathematical description of the *critical* purpose of all interferometers. The critical function of the interferometer is to convert high-frequency radiation into low-frequency signals that can be measured. High-frequency IR light ($\sim 10^{14}$ Hz) entering the interferometer is modulated into a strobe-like fringe frequency f. From Eq. (6c) this fringe frequency f is unique for each $\bar{\nu}$ emitted. The mirror velocity (typically near 0.16 cm/sec for the mid-IR range) of rapid-scanning interferometers produce modulated frequencies f in the audio frequency range (11). Detector response is dependent on f, and therefore the mirror velocity is a user controlled parameter. In general, the TGS detector response decreases with increasing mirror velocity (i.e., increasing f); however, the MCT detector response increases with increasing mirror velocity (i.e., increasing f) (11). Therefore mirror velocity is set higher for the MCT detector when compared to the TGS detector.

In practice, typical interferograms rapidly decay as the mirror moves away from either side of the ZPD as shown in Fig. 2B. When the fixed and moving mirrors depicted in Fig. 1 are of equal path length (i.e., zero optical retardation), *all wavelengths* of infrared light from the source are in phase

and the interferogram elicits a maximum amplitude and maximum constructive interference occurs. Thus at ZPD the maximum optical throughput occurs for both polychromatic and monochromatic IR sources and maximum amplitude is expected. However as the mirror travels away from ZPD, *individual* $\bar{\nu}$ *cosine waves* are increasingly out of phase with one another. This results in greater destructive interference between the $\bar{\nu}$ cosine waves and this causes the interferogram to decay rapidly. Experimentally, there is usually a small optical phase shift near ZPD, and consequently most measured interferograms are asymmetric in this region (14).

Equation (2) [or Eq. (4)] is a general function that describes interferograms for specific wavelengths of light, and consequently when multiple $\bar{\nu}$ enter an interferometer, the measured interferogram is described by the use of Eq. (2) [or Eq. (4)] for each $\bar{\nu}$ emitted. In other words, Eq. (2) applied to each $\bar{\nu}$ emitted is summed to give the interferogram of a broadband IR source (i.e., the superposition principle applies to the optical waves contributing to the interferogram). Consider mathematically describing one data point in the actual interferogram produced by a broadband IR source (e.g., Fig. 2B) at a fixed mirror position $x = L$ (the maximum optical retardation). In order to describe numerically the *intensity* of light reaching the detector at the mirror displacement equal to L cm [i.e., $I(L)$], Eq. (3) must be summed over all $\bar{\nu}$ emitted by the source and averaged over all wavelengths of light sampled (11,15),

$$I(L) = \sum_{i=0}^{k} B(\bar{\nu})_i \cos(2\pi\bar{\nu}_i L) \tag{7}$$

We emphasize that the movable mirror is fixed in this hypothetical example, and only one data point is being mathematically described in the total interferogram. In Eq. (7), L is constant and $\bar{\nu}_i$ and $B(\bar{\nu})_i$ are the ith wavelength and intensity of this wavelength being measured at the detector. To describe *completely* the interferogram produced by a typical IR source during a complete scan, one merely uses Eq. (7) for each mirror position associated with data acquisition. In other words, instead of calculating $I(L)$ at the maximum mirror displacement L (which is a constant), experimental interferograms require $I(x)$ for all possible mirror positions x (which is a variable). Data acquisition occurs at multiple discrete mirror positions, and for each mirror position, Eq. (7) can be used to calculate $I(x)$. Thus the general form of Eq. (7), for any particular mirror position associated with data acquisition, is

$$I(x) = \sum_{i=0}^{k} B(\bar{\nu})_i \cos(2\pi\bar{\nu}_i x) \tag{8}$$

or, in integral form (11,15),

$$I(x) = \int_{\bar{\nu}=0}^{\bar{\nu}=\infty} B(\bar{\nu}) \cos(2\pi\bar{\nu}x) d\bar{\nu} \tag{9}$$

where the limits of integration reflect an infinite spectrum.

Unfortunately $I(x)$ is *experimentally* measured and the integral given in Eq. (9) is merely a mathematical description of what is actually measured. In fact because $I(x)$ is experimentally measured, the desired spectral information $B(\bar{\nu})$ is mathematically obtained from this measured interferogram using the cosine Fourier transform of Eq. (9), which is

$$B(\bar{\nu}) = \int_{x=-\infty}^{x=\infty} I(x) \cos(2\pi\bar{\nu}x) dx \tag{10}$$

where the limits are for infinite mirror displacement.

Finite Mirror Displacement

Consider again a monochromatic light source emitting a single IR wavelength $B(\bar{\nu})$. Only one computer calculation using Eq. (10) would be required to describe $B(\bar{\nu})$ (i.e., the entire spectrum). However, it is not possible to calculate $B(\bar{\nu})$ from Eq. (10) because the integration limits require infinite mirror displacement. It is impossible to move the mirror infinite distances, and consequently Eq. (10) must be rewritten

$$B(\bar{\nu}) = \int_{x=-\infty}^{x=\infty} I(x) D_g(x) \cos[2\pi\bar{\nu}x] dx \tag{11}$$

where $D_g(x)$ has the value of 1 during the scan, $|x| \leq |L|$, and the value of zero after the scan, $|x| > |L|$, where L defines the maximum mirror displacement. In other words, before integration, the function "$I(x) \cos[2\pi\bar{\nu}x]$" in the above integral is multiplied by 0 at distances corresponding to $|x| > |L|$. This allows the integral to maintain the limits that approach infinity to satisfy the Fourier transform requirement, and the $D_g(x)$ function accounts for the physical limitation of finite mirror movement. Since the interferogram $I(x)$ is measured with finite mirror movement $x = \pm L$ cm, the resulting IR spectrum will have a finite resolution of $1/L$ cm^{-1}.

The key concept in Eq. (11) is that multiplication of each measured interferogram data point $I(x)$ by $D_g(x)$ occurs before integration, i.e., before calculating $B(\bar{\nu})$ intensities. $D_g(x)$ is denoted as an *apodization* function. We emphasize that $D_g(x)$ is a function that can depend on the value of x and that $D_g(x)$ need not have the value either 1 or 0 as described above, and in fact, $D_g(x)$ is usually a continuous function of x. Any one of approximately eight apodization functions are routinely used in infrared spectroscopy during data acquisition. For condensed phase spectra the choice of apodization function usually does not significantly influence the final band shape because the natural IR bandwidth is much greater than the bandwidth associated with the apodization function. However, for deconvolution of condensed phase spectra, the deconvolved IR spectrum can be severely distorted if the appropriate apodization function is not used. Thus apodization functions are used during the calculation of IR spectra from the experimentally measured interferograms, and apodization functions are used during the deconvolution of IR spectral lines.

The distortion of IR spectral lineshapes caused by apodization functions is best illustrated using the interferogram produced by a monochromatic light source, i.e., the cosine interferogram in Fig. 3A. The triangular apodization function described by the equation $D_g(x) = 1 - x/L$ is shown in Fig. 3B. The triangular apodization function is a triangle with its apex located at $x = 0$ and the base ranging from $-L$ cm to L cm. The multiplication of $D_g(x)$ with $I(x)$ results in a triangular-shaped interferogram $I(x)D_g(x)$ shown in Fig. 3C.

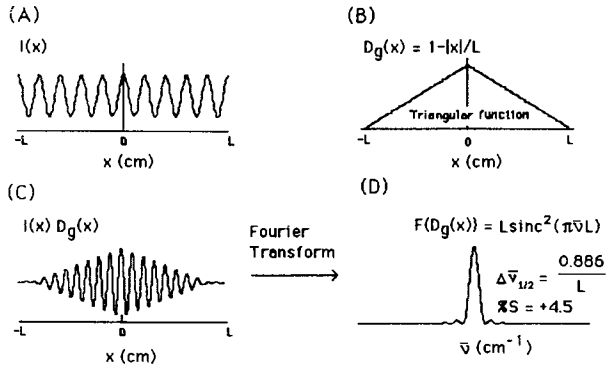

Fig. 3. An apodization function $D_g(x)$ changes the interferogram profile and the lineshape of the corresponding spectrum. The interferogram $I(x)$ of a monochromatic light source (A) and the triangular apodization function $D_g(x)$ shape (B) are multiplied together, resulting in an interferogram (C) described by $I(x)$ $D_g(x)$. The Fourier transformation of this interferogram results in a spectral lineshape (D) described by the apodization function lineshape $F[D_g(x)]$. The % S value equals the intensity of the first side lobe divided by the peak intensity multiplied by 100.

Thus multiplying the monochromatic light-source interferogram $I(x)$ by an apodization function $D_g(x)$ causes the profile of the interferogram to resemble the shape of the apodization function. In this example, Fourier transformation of the triangularly apodized monochromatic interferogram (Fig. 3C) using Eq. (11) results in an IR lineshape described by the equation $F[D_g(x)] = L\text{sinc}^2(\pi\bar{\nu}L)$ shown in Fig. 3D. In other words, for this very narrow input frequency, a monochromatic light source, the IR spectrum has bands with the lineshape dominated by the Fourier transformation of the apodization function $D_g(x)$. When the instrumental resolution is 4 cm^{-1} (i.e., $L = 0.25$ cm), the IR linewidth in Fig. 3D (calculated as $\Delta\bar{\nu} = 0.886/L$ for this apodization function) is approximately 3 cm^{-1}. Thus a monochromatic IR light source is always measured with a bandwidth approximately equal to the instrumental resolution regardless of the apodization function. Apodization functions differ significantly regarding side-lobe intensity and Fig. 3D shows that the triangular apodization function has only positive side lobes. Other apodization functions, e.g., boxcar and trapezoidal, have large negative side lobes. The bandshapes and side-lobe intensities of several apodization functions are given in Refs. 4, 8, and 11.

The IR Spectrum

Equation (11) emphasizes that $B(\bar{\nu})$ is the amplitude of a *particular* $\bar{\nu}$ calculated by a computer using all data points in the experimentally measured interferogram. From Eq. (11) it is clear that IR spectral information is encoded in the interferogram $I(x)$ but integration over all values of x is required even for a single $\bar{\nu}$. Typically IR sources emit polychromatic light and each wavelength of light emitted has a different intensity. A plot of this polychromatic IR source versus $\bar{\nu}$ is called a single-beam (SB) spectrum. Thus in order to obtain the single-beam spectrum from a polychromatic source emitting $\bar{\nu}$ between 4000 and 400 cm^{-1} (the midinfrared region), the same integration process described by Eq. (11) is performed for each $\bar{\nu}$ emitted. Evaluating Eq. (11) from $\bar{\nu}$ = 4000 to $\bar{\nu}$ = 400 cm^{-1} requires Eq. (11) to be rewritten as a double integral. Thus for a polychromatic IR source the SB spectrum is calculated from

$$\text{SB} = \int_{\bar{\nu}=400}^{\bar{\nu}=4000} \int_{x=-\infty}^{x=\infty} I(x)D_g(x)\cos(2\pi\bar{\nu}x)d\nu\,dx \qquad (12)$$

Equation (12) merely calculates the intensity of light $B(\bar{\nu})$, given by Eq. (11), for each $\bar{\nu}$ from 4000 to 400 cm^{-1} for all mirror displacements $x = -L$ cm to $x = L$ cm. When a sample is placed in the optical path the single-beam spectrum decreases in intensity at IR wavelengths absorbed by the sample. The percentage of transmitted IR light through the sample, % $T(\bar{\nu})$, is thus calculated from the single-beam spectra obtained with and without the sample in the optical path of the spectrometer

$$\%\ T(\bar{\nu}) = \frac{\text{SB}_{\text{sample}}}{\text{SB}_{\text{background}}} \times 100 \qquad (13)$$

where $\text{SB}_{\text{sample}}$ is the single-beam spectrum obtained with the sample in the light path and $\text{SB}_{\text{background}}$ is the single-beam spectrum without the sample in the light path. The absorbance spectrum $A(\bar{\nu})$ is calculated from % $T(\bar{\nu})$ by

$$A(\bar{\nu}) = -\log[\%\ T(\bar{\nu})/100] \qquad (14)$$

In FTIR spectroscopy, plotting data in absorbance units "$A(\bar{\nu})$," in contrast to percentage transmittance "% $T(\bar{\nu})$," is preferred because data manipulation such as spectral subtraction is possible only in the absorbance mode (16,17). The experimental requirements for obtaining % $T(\bar{\nu})$ and $A(\bar{\nu})$ are depicted in Figs. 4 and 5.

A few final comments on producing a single-beam spec-

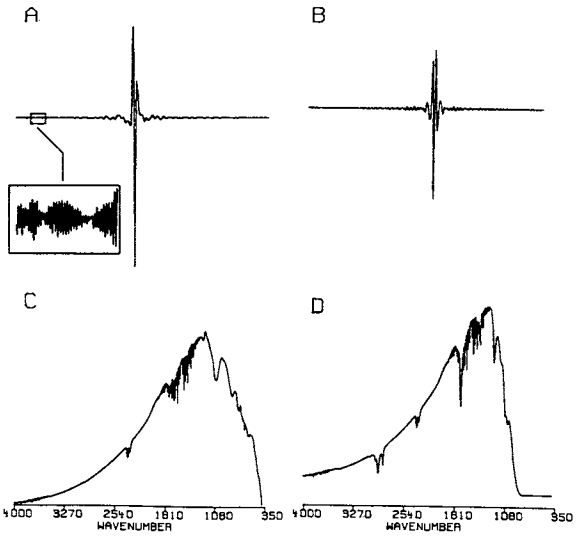

Fig. 4. Obtaining an experimental infrared spectrum of a sample requires measuring two interferograms: (A) the background interferogram and (B) the sample interferogram. These interferograms were Fourier transformed into their corresponding single-beam spectra shown below each interferogram (C and D) through the use of Eq. (12). The inset to the background interferogram (A) shows the spectral information in the wings of the interferogram. The sample single-beam spectrum is a dilauroylphosphatidylcholine lipid film on a CaF_2 plate (19). Sharp water vapor and carbon dioxide bands are apparent in both single-beam spectra.

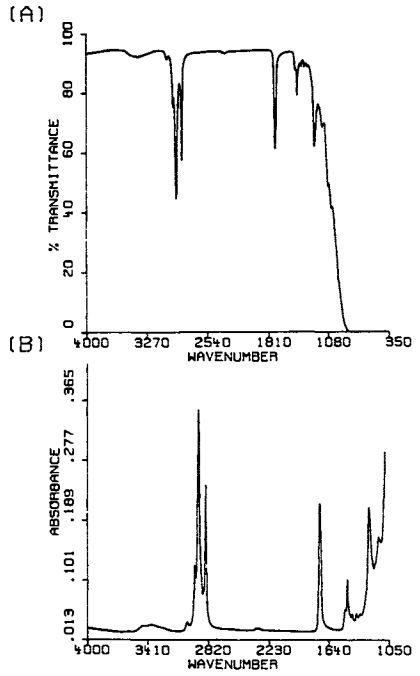

Fig. 5. Transmission spectrum (A) and corresponding absorbance spectrum (B) obtained from the single-beam spectra in Fig. 4. The sample spectrum is a dilauroylphosphatidylcholine lipid film on a CaF_2 plate (19). The percentage transmittance % $T(\bar{\nu})$ is calculated using Eq. (13), which takes the ratio of the single-beam spectra of a broadband source measured with (Fig. 4D) and without (Fig. 4C) the sample present. The absorbance spectrum $A(\bar{\nu})$ is subsequently calculated from the % $T(\bar{\nu})$ spectrum using Eq. (14).

trum by calculating each $B(\bar{\nu})$ using the numerical form of equation (11) are needed. Interferograms, in theory, are symmetrical on both sides of ZPD and therefore it is convenient to expand Eq. (11),

$$B(\bar{\nu}) = \int_{x=-\infty}^{x=0} I(x)\, D_g(x) \cos[2\pi\bar{\nu}x]dx + \int_{x=0}^{x=\infty} I(x)D_g(x) \cos[2\pi\bar{\nu}x]dx \qquad (15)$$

Based on the integral limits, these integrals merely calculate the area on each side of ZPD. This is graphically shown in Fig. 2 for both interferograms. The area on each side of ZPD (i.e., $x = 0$) are equal because the cosine functions in the above integrals are even functions, that is, $I(-x) = I(x)$. Because the integrals are equal, Eq. (15) can be rewritten as

$$B(\bar{\nu}) = 2 \int_{x=0}^{x=\infty} I(x)D_g(x) \cos[2\pi\bar{\nu}x]dx \qquad (16)$$

where the integral limits are now the mirror displacement x for a single-sided scan. Based on Eq. (16), a single-sided scan (mirror movement from 0 to L cm) generates a single-sided interferogram, whereas a double-sided scan (mirror movement from $-L$ to $+L$ cm) generates a double-sided interferogram, but both interferograms provide the same spectral information. Data collection for both double-sided interferograms and single-sided interferograms occurs as the mirror moves away from the beam splitter. Thus as the movable mirror travels in the forward direction, data collection occurs (see Fig. 1). For a fixed number of scans, double-sided interferograms provide better signal-to-noise ratios than single-sided scans because the spectral information is sampled twice (once on each side of ZPD). However, obtaining spectra from single-sided interferograms allows a greater number of scans per second, which is useful for *gas phase* experiments that require rapid data acquisition (e.g., GC/FTIR) (11,18). Single-sided interferograms begin data collection just to the left of ZPD to allow for phase correction (11).

Instrument Resolution and Spectral Noise

The instrumental resolution, δ_0, of IR bands depends solely on the maximum distance of mirror movement L,

$$\delta_0 = \frac{1}{L} \qquad (17)$$

where δ_0 is the instrumental resolution in cm^{-1}. As L increases the optical retardation increases [Eq. (3)] and the resolution at which the IR data are obtained increases [Eq. (17)]. Unfortunately, as L increases, the amount of *spectral noise* increases. Spectral noise increases because during a complete scan, electronic and instrument noise remains constant, whereas the signal decays or decreases (Fig. 4A); therefore the S/N of the interferogram decreases as the mirror is displaced further from the ZPD. Equation (10) demonstrated that every $I(x)$ value in the interferogram is used to calculate each $B(\bar{\nu})$ in the single beam spectrum. Thus as L increases, i.e., S/N decreases, more interferogram noise causes all IR frequencies to have increased spectral noise. Measured interferograms decay rapidly with increasing mirror movement beyond ZPD, but at some finite mirror position, little (or no) IR signal exists and the detector is recording only noise. If the detector is recording mostly noise because the optical retardation is too high, the instrument resolution should be decreased to acquire the data. In other words, the S/N depends on the instrument resolution, and when the maximum mirror displacement causes the spectral signal intensity to be equal to or less than the instrumental-noise intensity, IR data should not be measured.

It is important to avoid high-resolution IR scans when the actual condensed phase spectra exhibit naturally wide IR bands. High resolution requires the movable mirror to travel excessive distances to obtain sufficient optical retardations for the high resolution. Measurement of condensed phase spectra at high resolution increases noise in the spectrum as described above, and this limits the ability to deconvolve IR spectral lines. For condensed phase spectra, it is rarely necessary to measure spectra at resolution greater than 2 cm^{-1}, and typically 4-cm^{-1} resolution is acceptable. To determine the optimum resolution for a particular condensed phase sample, one merely obtains IR spectra at low, intermediate, and high resolution to determine when the spectral noise is apparent in the broad IR bands. Alternatively, obtaining one high-resolution interferogram can yield all the information needed to identify the desired resolution. Prior to Fourier transformation to obtain the SB spectrum, the high-resolution interferogram is merely truncated at mirror positions corresponding to lower instrument resolution. In other

words, the interferogram is measured with a constant amount (in fact an excessive number of) data points, but the number of transform points, used to obtain the SB spectrum, is reduced to obtain a low-resolution spectrum. Thus one high-resolution interferogram can be Fourier transformed several times at sequentially lower resolutions by truncating the measured interferogram prior to Fourier transformation. Obviously the high-resolution interferogram would have to be stored as a separate computer file for this experiment.

CONVOLUTION THEORY

Resolution of unresolved IR bands requires deconvolution. Before applying deconvolution to IR spectra, it is critical to understand the inverse process of deconvolution, which is convolution. As briefly described under Finite Mirror Displacement, the experimentally observed IR bandshape $A(\bar{\nu})$ is the convolution of the apodization function and intrinsic or natural IR bandshape. Convolution (denoted by $*$) of the intrinsic IR lineshape with the instrumental lineshape is given by

$$A(\bar{\nu}) = E_0(\bar{\nu}) * W_0(\bar{\nu}) \qquad (18)$$

where the instrumental lineshape $W_0(\bar{\nu})$ is actually the apodization function $D_g(x)$ and the intrinsic lineshape $E_0(\bar{\nu})$ is produced by molecular vibrations. Thus all observed IR bands are actually the convolution of two functions, and consequently all experimentally measured IR bands are broader and less intense relative to the true IR band. Inherent to the convolution process of two functions are decreased peak intensity and increased peak width.

A simple example demonstrates that convolution is merely a matrix multiplication of one function sliding through another function (Fig. 6) (6,20). In this example an idealized IR band with a triangular lineshape $E_0(\bar{\nu})$, peak height of 3 ordinate units, half-bandwidth of 3 units, and band area of 9 units is used. The instrumental lineshape $W_0(\bar{\nu})$ is a boxcar apodization function with a half-bandwidth of 1 unit and a height of 2 units. The boxcar function is initially centered at the -4 abscissa position, where the leading edge of the boxcar function coincides with the beginning of the triangular band. The convolution process can be visualized to occur by unit abscissal steps of the boxcar as shown on the right in Fig. 6. The convolution matrix multiplication is achieved by multiplying the intensity of each boxcar element (i.e., 2) with the intensity of each triangular band element (i.e., the numbers in bold parentheses) at each unit abscissal position and this value is given in parentheses in the matrix table above the boxcar element intensity. For each boxcar position, Σ is the $A(\bar{\nu})$ convolved band intensity prior to normalization for band areas. Convolution does not change band areas, and therefore these summed values must be normalized to produce a convolved band with a band area equal to the original triangular band. The normalized ordinate values of the convolved band $A(\bar{\nu})$ are listed in the column labeled Σ/N. The normalization factor 9/54 was obtained by dividing the band area before matrix multiplication by the band area after matrix multiplication. It is evident from Fig. 6 that the convolved band $A(\bar{\nu})$ exhibits a bandwidth greater than $E_0(\bar{\nu})$ (2 units) and the peak height intensity is 0.7 units less than $E_0(\bar{\nu})$. Although not obvious from

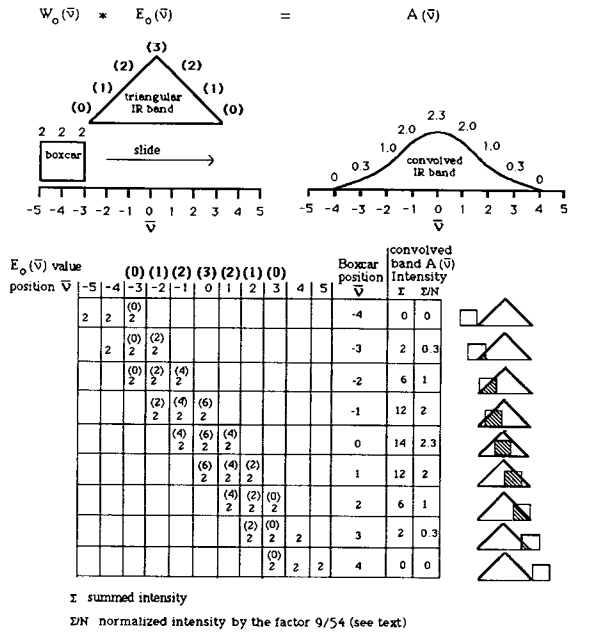

Fig. 6. Graphical illustration that demonstrates convolution is the matrix multiplication of one function sliding through another. In this case the convolution of a triangular-shaped IR band $E_0(\bar{\nu})$ with boxcar apodization function $W_0(\bar{\nu})$ to form the observed IR band $A(\bar{\nu})$ is depicted. The convolved band $A(\bar{\nu})$ has a decreased band intensity, an increased bandwidth, and an equivalent band area relative to $E_0(\bar{\nu})$ (6,20).

the graph, the total area under $A(\bar{\nu})$ remains the same as $E_0(\bar{\nu})$ in Fig. 6.

The intention of Fig. 6 was to demonstrate both the process of convolution and the difference between measured and intrinsic bandshapes. When measuring an IR band, the intrinsic IR line shape is not measured, but rather an instrumentally observed IR band shape is measured. For describing the process of convolution in the frequency domain, we used a boxcar apodization function, but other apodization functions could have been used. However, triangular IR bands do not exist and the convolved boxcar-IR band in Fig. 6 (upper right) is unrealistic. In practice the intrinsic IR lineshape $E_0(\bar{\nu})$ of condensed phase spectra is best described as a combination of both Lorentzian and Gaussian lineshapes at the ratio of 90:10 (6). However, $E_0(\bar{\nu})$ is usually simplified to only a Lorentzian function as shown in Fig. 7 (2,3,5,6). A single IR band exhibiting a Lorentzian lineshape can be described by Eq. (19) (2,3,5,6)

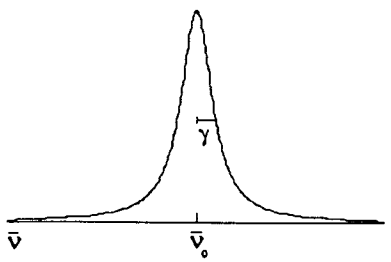

Fig. 7. The Lorentzian lineshape is the simplified band profile of condensed phase infrared spectra.

$$A(\bar{\nu}) = A_{peak}\{\gamma^2/[\gamma^2 + (\bar{\nu} - \bar{\nu}_0)^2]\} \quad (19)$$

where $A(\bar{\nu})$ is the absorbance at wavenumber $\bar{\nu}$, A_{peak} is the maximum absorbance of the band centered at $\bar{\nu}_0$, and γ is the half-width at half-height (HWHH) of the band. For condensed phase spectra, the instrumental resolution is generally much higher than the spectral resolution γ. In other words, when $\delta_0 \ll \gamma$, *the contribution of the instrumental lineshape* $W_0(\bar{\nu})$ *to the observed lineshape* $A(\bar{\nu})$ *can frequently be neglected* unless the IR bands are subjected to Fourier self-deconvolution. Fourier deconvolution can reduce the observed IR bandwidth(s) enough to cause the deconvolved bandwidth(s) to be determined by the Fourier transformation of the instrumental lineshape function or $F[D_g(x)]$.

THEORY OF FOURIER DECONVOLUTION

IR bands from condensed phase samples are typically broad and convolved with an instrumental lineshape function that further broadens the IR bands. Frequently, IR instruments cannot resolve these broad overlapping bands. Increasing the instrumental resolution will merely result in more data points in the IR bands that remain unresolved, and this is the meaning of *instrumentally unresolved* IR bands. Fourier deconvolution can be used to resolve (at least in part) the overlapping IR bands by both reducing the observed IR bandwidth and increasing the IR peak height without changing the peak position. These deconvolved IR bands facilitate identifying the actual number of IR bands, and the IR band peak positions.

The process of obtaining experimental IR spectra is pictorially summarized in Fig. 8. The experimentally measured interferograms for both the sample and the background are shown. Fourier transformation of these interferograms by Eq. (12) gives a single-beam spectra for each interferogram. The function $I(x)$ and its transform SB exist in two different domains; $I(x)$ exists in the distance domain (units of cm), and SB exists in the frequency or wavenumber domain (units of cm^{-1}). Figure 8 demonstrates that in the frequency domain, two single-beam spectra were divided to obtain the percentage transmittance spectrum, which is converted to an absorbance $A(\bar{\nu})$ spectrum by Eq. (14). For Fourier transform pairs, the convolution theorem states (21) that

(i) convolution of two functions means multiplication of their transforms and
(ii) deconvolution of two functions means division of their transforms.

In other words, multiplication of two functions in one domain is convolution of those functions in the other domain. Similarly, the division of two functions in one domain is equivalent to deconvolution of those functions in the other domain. $I(x)$ and SB are Fourier transform pairs. In order to obtain the absorbance spectrum $A(\bar{\nu})$ in Fig. 8, the sample and background single-beam spectra were *divided* in the frequency domain. This division resulted in the removal of the background information in the experimentally measured spectrum. Fourier transformation of this absorbance spectrum $A(\bar{\nu})$ gives a single-sided *artificial interferogram* $I'(x)$ as shown in Fig. 8. The term artificial in artificial interferogram merely emphasizes that this interferogram is calculated from

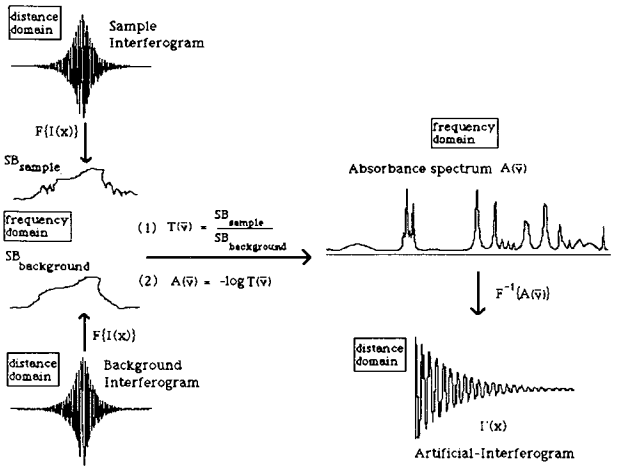

Fig. 8. A schematic demonstrating how experimental IR spectra are obtained. Double-sided interferograms $I(x)$ are measured with and without the sample in the light path, producing the sample (top) and background (bottom) interferograms, respectively. These interferograms are Fourier transformed $F[I(x)]$ to give the corresponding single-beam spectra of the sample SB_{sample} and the background $SB_{background}$. Division of the single-beam spectra $SB_{sample}/SB_{background}$ results in a sample spectrum in percentage transmittance $T(\bar{\nu})$ and converting to an absorbance spectrum $A(\bar{\nu})$ by taking the $-\log T(\bar{\nu})$. The absorbance spectrum $A(\bar{\nu})$ can be Fourier transformed $F^{-1}\{A(\bar{\nu})\}$ to an artificial-interferogram $I'(x)$ which is a calculated single-sided interferogram that does not contain background spectral information.

a Fourier transformation, and not measured. However, we emphasize that this single-sided artificial interferogram $I'(x)$ is much different than either the sample or the background double-sided interferograms because of the division of the single-beam spectra in the frequency domain. Because the background information was removed by division in the frequency domain $A(\bar{\nu})$, the background information was deconvolved in the distance domain $I'(x)$. In other words, since background information is absent from the IR absorbance spectra, then background information is absent from the artificial interferogram.

Conversion of the measured IR spectrum into an artificial interferogram shown in Fig. 8 is somewhat misleading. Fourier transformation of an entire absorbance spectrum from 4000 to 400 cm^{-1} would require excessive computer time and computer space. Usually, narrow spectral regions, 50–100 cm^{-1} wide, have molecular vibrations from similar functional groups, and consequently similar IR bandwidths are expected in narrow regions of the spectrum. Typically only a part of the spectrum is used for deconvolution (5). Consider a narrow region of an IR spectrum $A(\bar{\nu})$ from $\bar{\nu}_1$ to $\bar{\nu}_2$ cm^{-1} that contains a *single* IR band described by a Lorentzian lineshape exhibiting the A_{peak} at $\bar{\nu}_0$. The inverse Fourier transform of this IR region denoted by $F^{-1}[A(\bar{\nu})]$ calculates an artificial interferogram $I'(x)$,

$$I'(x) = F'[A(\nu)] = 0.5\ \gamma A_{peak} \exp(-2\pi\gamma x) \cos(2\pi\bar{\nu}_0 x) D_g(x) \quad (20)$$

$I'(x)$ is composed of four terms: $0.5\gamma A_{peak}$, which is proportional to the band area; $\cos(2\pi\bar{\nu}_0 x)$, which contains the IR frequency $\bar{\nu}_0$; $\exp(-2\pi\gamma x)$, which controls the exponential

decay of the artificial interferogram; and the apodization function $D_g(x)$, used to truncate the artificial interferogram at $x > L$ cm (2,3,5,6). In Eq. (20), $\exp(-2\pi\gamma x)$ contains the constant γ, which controls the exponential rate of decay of the artificial interferogram. In other words, γ in the frequency domain determines the exponential decay in the distance domain of $I'(x)$. The rate of decay of $I'(x)$, shown in Fig. 9, can be reduced by dividing the artificial interferogram by a function $\exp(-\gamma' x)$, where $\gamma' \leq \gamma$.

$$I'(x) = 0.5\ \gamma A_{peak} \frac{\exp(-2\pi\gamma x)}{\exp(-\gamma' x)} \cos(2\pi\bar{\nu}_0 x) D_g(x) \quad (21)$$

Thus when the artificial interferogram shown in Fig. 9 is divided by $\exp(-\gamma' x)$, this has the effect of reducing the exponential decay of the interferogram as shown in Fig. 10. Figures 9 and 10 are plotted on the same scale and thus the decreased rate of decay of $I'(x)$ is apparent in Fig. 10. Since division of functions in one domain results in deconvolution in the other domain, dividing the artificial interferogram [i.e., Eq. (20)] by $\exp(-\gamma' x)$ in the distance domain results in *deconvolution* of the spectrum in the frequency domain. The exponential terms in Eq. (21) can be combined,

$$I'(x) = 0.5\ \gamma A_{peak} \exp[-2\pi(\gamma - \gamma')x] \cos(2\pi\bar{\nu}_0 x) D_g(x) \quad (22)$$

which shows that the exponential decay of $I'(x)$ is determined by $\gamma - \gamma'$. Since $\gamma - \gamma'$ is less than γ, then $I'(x)$ decays more slowly and the new half-bandwidth in the IR spectrum is $\gamma - \gamma'$. Thus the key term in Eq. (22) is $(\gamma - \gamma')$, which controls in part the final half-bandwidth in the IR spectral region of interest, along with the apodization function $D_g(x)$. The deconvolved spectrum $A'(\bar{\nu})$ is obtained by performing the Fourier transform operation $F[I'(x)]$,

$$A'(\bar{\nu}) = F[I'(x)] \quad (23)$$

which results in the deconvolved spectrum from $\bar{\nu}_1$ to $\bar{\nu}_2$ cm^{-1} as shown in Fig. 10.

In summary, Fourier deconvolution of an IR spectral region (illustrated in Figs. 9 and 10) is accomplished by (i) generating an artificial interferogram $I'(x)$ that describes the spectrum $A(\bar{\nu})$, in the region of interest $\bar{\nu}_1$ to $\bar{\nu}_2$ cm^{-1}, using the inverse Fourier transform operation $F^{-1}[A(\bar{\nu})]$; (ii) smoothing the artificial interferogram with an apodization function $D_g(x)$ (Fig. 9); (iii) dividing the artificial interferogram by an exponential weighting function $\exp(-\gamma' x)$; and (iv) Fourier transformation $F[I'(x)]$, which gives the deconvolved spectrum $A'(\bar{\nu})$ containing an infrared band(s) with a decreased bandwidth (Fig. 10). As shown in Eq. (22) the HWHH of the deconvolved band is $\gamma - \gamma'$.

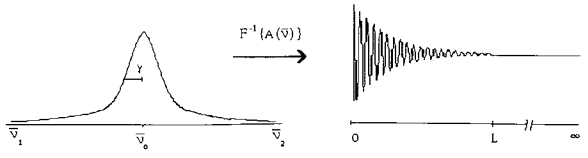

Fig. 9. An artificial interferogram is generated from a narrow region of the IR spectrum, from $\bar{\nu}_1$ to $\bar{\nu}_2$ cm^{-1}. This example shows a Lorentzian-shaped band which also has the contribution of an apodization lineshape function $F[D_g(x)]$, where $D_g(x)$ is used to truncate the artificial interferogram at L cm. $A(\bar{\nu})$ and $I'(x)$ are Fourier transform pairs where the artificial interferogram $I'(x)$ is calculated from the spectrum $A(\bar{\nu})$ by the inverse Fourier transform operation $F^{-1}[A(\bar{\nu})]$ using the equation above $I'(x)$.

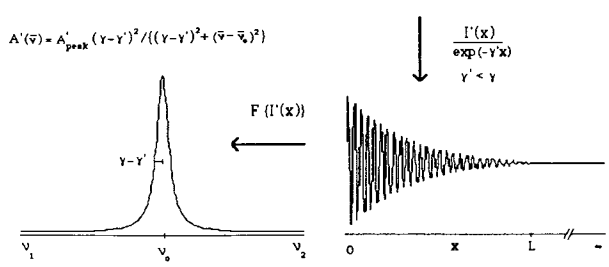

Fig. 10. The artificial interferogram shown in Fig. 9 is weighted by $1/\exp(-\gamma' x)$ to reduce the rate of decay. The resulting Fourier transformation to the frequency domain by the operation $F[I'(x)]$ results in a deconvolved spectrum $A'(\bar{\nu})$. This deconvolved spectrum is described by a half-bandwidth $(\gamma - \gamma')$, which is smaller than the original half-bandwidth γ and a peak height A'_{peak}, which is a factor $\gamma/(\gamma - \gamma')$ higher than the original peak height A_{peak}.

COMPLETE VS PARTIAL DECONVOLUTION

Acceptable deconvolved IR bands may be either partially or completely deconvolved. Complete deconvolution means completely removing the intrinsic or natural lineshape from the measured IR band; consequently the apodization lineshape determines the IR band contour and all spectral information about the IR "lineshape" is lost. Complete or maximum spectral deconvolution occurs when $\gamma = \gamma'$ because the term $\exp[-2\pi(\gamma - \gamma')x]$ in Eq. (22) equals 1, and the weighted artificial interferogram is a pure/infinite cosine wave shown in Fig. 3A. Apodization of a pure cosine wave with $D_g(x)$ caused the lineshape to be dominated by $F[D_g(x)]$ in the frequency domain (Fig. 3D). This is more clearly illustrated by substituting $\gamma = \gamma'$ into Eq. (22), which gives

$$I'(x) = 0.5\ \gamma A_{peak} \cos(2\pi\bar{\nu}_0 x) D_g(x) \quad (24)$$

The deconvolved spectra is obtained by performing the Fourier transformation of Eq. (24). Using a triangular apodization function $[D_g(x) = 1 - x/L]$, the Fourier transformation of Eq. (24) is

$$A'(\bar{\nu}) = A'_{peak}\ L\ \mathrm{sinc}^2\{\pi(\bar{\nu} - \bar{\nu}_0)]L\} \quad (25)$$

where the $L\mathrm{sinc}^2$ term is from the Fourier transformation of the triangular apodization function.

Complete deconvolution is illustrated using an idealized spectrum $A(\bar{\nu})$ with a Lorentzian bandshape (Fig. 11A). The inverse Fourier transform operation $F^{-1}[A(\bar{\nu})]$ is performed producing the artificial interferogram $I'(x)$ which contains the spectral information in the region of interest (Fig. 11B). This calculated artificial interferogram is *multiplied* (convolved) with a triangular apodization function $D_g(x)$ and *divided* (deconvolved) with a function $\exp[-\gamma'|x|]$ which completely removes the exponential decay attributed to the Lorentzian IR lineshape function. This results in an artificial interferogram whose profile is determined by only the apodization function (Fig. 11C). The deconvolved spectrum $A'(\bar{\nu})$ is generated by the Fourier transform operation $F[I'(x)]$

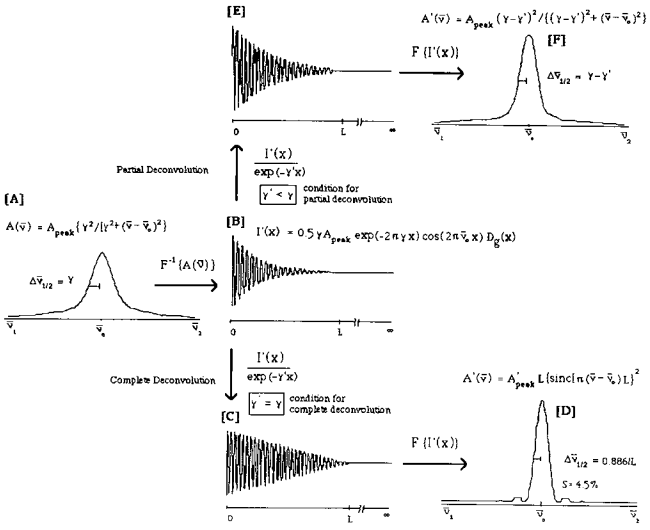

Fig. 11. Examples of complete and partial spectral deconvolution. The IR spectrum (A) is Fourier transformed to give $I'(x)$ as shown in B. $I'(x)$ is then divided by a weighting function $\exp[\gamma'|x|]$ to remove completely the natural linewidth (C) or remove partially the natural linewidth (E) from the interferogram. Fourier transformation of the interferograms produces infrared spectrum that are completely (D) or partially (F) deconvolved. Prior to deconvolution, the observed bandwidth is γ, and after deconvolution the bandwidth equals $\gamma - \gamma'$ for partial deconvolution. For complete deconvolution the observed bandwidth equals $0.886/L$ when using the apodization function shown; other apodization functions will change this calculation.

(Fig. 11D). After deconvolution, the band intensity (A'_{peak}) has increased because the band area remains unchanged by deconvolution. Also note the appearance of side lobes in the deconvolved spectrum, which is indicative of an IR lineshape dominated by the apodization function.

Side lobes in deconvolved spectra limit the interpretation of IR spectra. Consequently it is more common to partially deconvolve spectral lines to avoid side lobes in the final spectrum. For partial deconvolution, the weighting function $1/\exp(-\gamma' x)$ is utilized under the condition $\gamma > \gamma'$ and this is also illustrated in Fig. 11. Note that during partial deconvolution, division of $I'(x)$ by $\exp(-\gamma' x)$ caused the artificial interferogram to maintain the appearance of exponential decay (Fig. 11E), and also note that the final spectrum does not contain side lobes (Fig. 11F). For partial deconvolution, the deconvolved IR band $A'(\bar{\nu})$ in Fig. 11F is given by (9)

$$A'(\bar{\nu}) = A'_{peak}\{\gamma - \gamma')^2/[(\gamma - \gamma')^2 + (\bar{\nu} - \bar{\nu}_0)^2]\} \quad (26)$$

Examples of Fourier Deconvolution

Most deconvolution programs require the input of four deconvolution parameters by the operator. These include the spectral region $\bar{\nu}_1$ to $\bar{\nu}_2$ cm^{-1}, the apodization function $D_g(x)$, γ_0 for the narrowest IR band of interest, and the resolution enhancement factor K. However, some deconvolution programs may also require an estimation of the lineshape composition in percentage Gaussian and Lorentzian (6). The resolution enhancement factor K is given by (5)

$$K = \frac{\gamma}{(\gamma - \gamma')} = \frac{A'_{peak}}{A_{peak}} \quad (27)$$

which demonstrates that the deconvolved peak height, A'_{peak}, has increased relative to the measured peak absorbance, A_{peak}, by a factor of K.

In practice the instrument resolution should be less than or equal to the deconvolved band full-width at half-height or substantial bandshape distortion occurs (9). For example, consider when the instrumental resolution δ_0 equals the deconvolved IR bandwidth

$$\delta_0 = 2(\gamma - \gamma') \quad (28)$$

Rearranging this equation gives

$$(\gamma - \gamma') = \delta_0/2 \quad (29)$$

Substituting Eq. (29) into Eq. (27),

$$K = \gamma/(\gamma - \gamma') = \gamma/(\delta_0/2) \quad (30)$$

where the maximum expected resolution enhancement factor K is now a function of the experimental resolution δ_0 cm^{-1} and the observed HWHH γ for the band of interest. For example, if a spectrum measured at 4-cm^{-1} resolution (i.e., $\delta_0 = 4$ cm^{-1}) contained overlapping bands with a HWHH of 10 cm^{-1} (the band had a full width of 20 cm^{-1} at half-peak maximum), the maximum resolution enhancement factor K according to Eq. (30) is 5; that is,

$$K = \gamma/(\delta_0/2) = 10/(4/2) = 5 \quad (31)$$

In practice, the use of large K values is usually not possible because deconvolution enhances noise in the measured spectrum. Consequently deconvolution of experimental spectra commonly use K values <5 and usually K values range between 1.5 and 2.5.

The first step in deconvolution is to determine δ_0, $(S/N)_0$, and γ of the measured spectrum. The S/N is determined by dividing the peak intensity in the region of interest by the peak-to-peak background noise. The baseline spectral region is used to monitor the noise level in the deconvolved spectra. It may be difficult to estimate γ because of overlapping bands, however, the correct estimation of γ is important for acceptable band deconvolution.

Figure 13A shows the IR spectrum of a dilauroylphosphatidylcholine lipid suspension obtained at 4-cm^{-1} resolution ($\delta_0 = 4$) by coadding 512 scans (22). The C–H stretching region (3000 to 2800 cm^{-1}) contains several overlapped bands due to the CH_2 asymmetric and symmetric stretching bands ($\bar{\nu}_{as}$ CH_2 and $\bar{\nu}_s$ CH_2) and CH_3 asymmetric and symmetric stretching bands ($\bar{\nu}_{as}$ CH_3 and $\bar{\nu}_s$ CH_3). After subtraction of the aqueous solvent (16,17,22), the lipid bilayer spectrum shows $\bar{\nu}_{as}$ CH_2 (2920 cm^{-1}) with a peak intensity of 0.1606 (Signal S) absorbance unit and a peak-to-peak noise intensity of 0.0003 (Noise N) absorbance unit (in the region near 3050 cm^{-1}). The signal-to-noise ratio $(S/N)_0$ of the measured spectrum is

$$(S/N)_0 = \frac{0.1606}{0.0003} = 535 \quad (32)$$

The extent to which deconvolution decreases S/N in the deconvolved spectrum [denoted (S/N)'] depends on both the

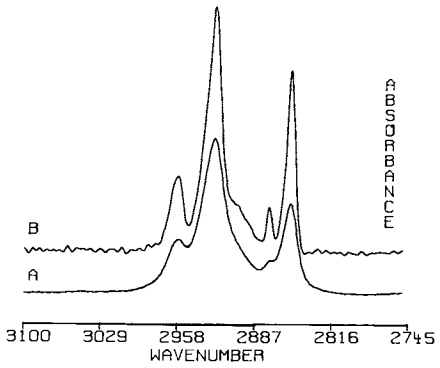

Fig. 12. Fourier deconvolution of the C–H stretching region of dilauroylphosphatidylcholine bilayers with a 10 cm^{-1} HWHH Lorentzian line. This spectrum was recorded with a Nicolet 20 SXC spectrometer using the cylindrical internal reflectance micro CIRCLE cell (Spectra-tech, Inc., Stamford, CT) accessory (22). The bilayers were formed by hydrating the lipid film with D_2O (22). Spectra for both D_2O and $diC_{12}PC/D_2O$ were obtained at 4 cm^{-1} resolution by coadding 512 interferograms (22). Subtraction of the D_2O solvent spectrum resulted in a difference spectrum of the $diC_{12}PC$ bilayers with a S/N $\approx$ 535 (16,17,22). (A) Experimental spectrum with an instrument resolution of 4 cm^{-1} and a signal-to-noise ratio S/N of about 535. (B) Deconvolved spectrum with a Bessel apodization function γ = 10 cm^{-1} and a K = 2.0.

resolution enhancement factor K and the apodization function. A general rule in deconvolution is that for each factor of two by which γ_0 is decreased (or the IR peak intensity is increased), (S/N)′ is reduced by a factor of about 10 (4,8,9). Therefore, during deconvolution, the appropriate choice of K should satisfy the condition (4,8)

$$K \leq \log(S/N) \tag{33}$$

The $\bar{\nu}_s$ CH_2 band at 2850 cm^{-1} is narrower than $\bar{\nu}_{as}$ CH_2 and thus the best estimate of the γ_0 is determined from the $\bar{\nu}_{as}$ CH_2 band. At one-half the peak intensity, γ equals 10 cm^{-1}. The ratio γ/δ_0 equals

$$\frac{\gamma}{\delta_0} = \frac{10}{4} = 2.25 \tag{34}$$

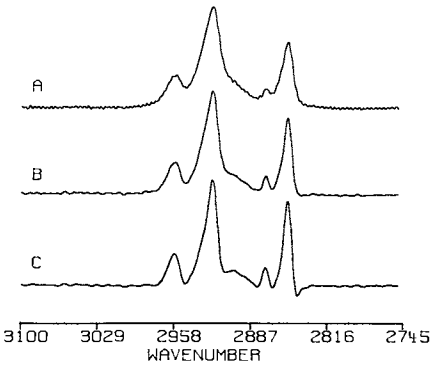

Fig. 13. Illustration of the effect of change in half-bandwidth values, γ, during deconvolution of IR spectra. The measured spectrum of dilauroylphosphatidylcholine bilayers from Fig. 12A was deconvolved with a Bessel apodization function and K = 2 using the following half-bandwidths: (A) γ = 5 cm^{-1}; (B) γ = 10 cm^{-1}; and (C) γ = 15 cm^{-1}.

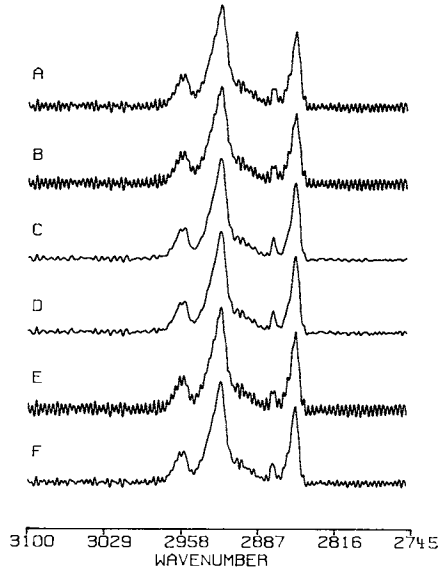

Fig. 14. Comparison of the effect of apodization function on the signal-to-noise ratio of deconvolved spectra. The measured IR spectrum of dilauroylphosphatidylcholine ($diC_{12}PC$) bilayers from Fig. 12A had $(S/N)_0$ = 535. The self-deconvolved spectra with K = 2.7 and a HWHH of 10 cm^{-1} show significant differences in (S/N)′ depending on the $D(x)$ used: (A) triangular/sinc; (B) triangular squared; (C) Bessel; (D) cosine; (E) Gaussian; and (F) sinc squared.

The maximum K is 2.7 calculated from Eq. (33). Thus a K value of 2.0 is a good first approximation. Using a Bessel apodization function, K = 2, and γ = 10 cm^{-1}, the deconvolved IR spectrum of dilauroylphosphatidylcholine bilayers is shown in Fig. 12B.

In practice, γ used for deconvolution is estimated from the measured IR spectrum. Usually visual inspection of the measured IR spectrum leads to poor approximations of γ,

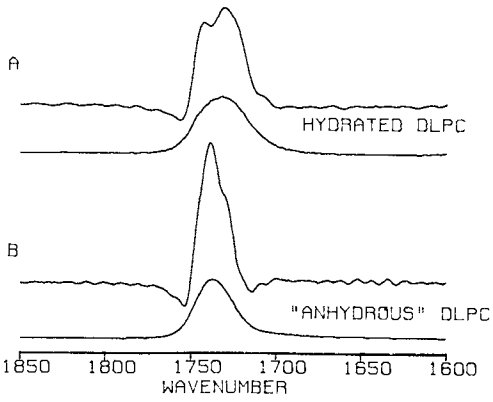

Fig. 15. An example whereby spectral information can be obtained only through the use of Fourier deconvolution. Deconvolution of C=O stretching region of the sn-1 and sn-2 carbonyl esters of completely hydrated dilauroylphosphatidylcholine ($diC_{12}PC$) bilayers (22) (A) and "anhydrous" $diC_{12}PC$ lipid film (19) (B). The original spectrum is of hydrated $diC_{12}PC$ bilayers as described in the legend to Fig. 12A. Deconvolution parameters for the hydrated lipid bilayer spectrum used a Bessel apodization function K = 2 and HWHH = 19 cm^{-1}. Deconvolution parameters for the "anhydrous" lipid film spectrum used a Bessel apodization function K = 2.75 and HWHH = 19 cm^{-1}.

TABLE I. Applications of Fourier Transform Infrared Spectroscopy in the Pharmaceutical Sciences[a]

Objective	Technique	Sample(s)	References
Direct analysis of powdered drugs from tablets and capsules	Diffuse reflectance (DRIFT)	Prazepam, meprobamate, glutethimide, methocarbamol, aspirin, methyprylon, caffeine mebutamate, carisoprodol, ethinamate, quaalude, valium, cocaine HCl, phencyclidine base, methamphetamine HCl, caffeine	25–27
Quantitation of lipid in membrane systems	Transmission/CaF_2 film	Phospholipids, cholesterol	19,28
Characterization and quantitation of silica-immobilized lipids	Infrared microscope reflectance mode	Phospholipids and fatty acids covalently bonded to silica	28–30
Conformational analysis and thermotropic behavior of membrane lipids	Attenuated total reflectance (ATR)/aqueous suspension	Phospholipids	22–24,28,31
Conformational analysis of peptides and proteins	ATR/aqueous systems	Membrane proteins, soluble proteins, peptide hormones, enzymes	6,32–34
Skin permeability enhancement	ATR and transmission	Stratum corneum, *n*-alkanols, oleic acid	35–37

[a] Literature surveys for infrared spectroscopy covering the period of 1982 to the end of 1989 can be found in the following: *Anal. Chem.*, 1986, 58:1906–1925; *Anal. Chem.*, 1990, 62:223R–255R; *J. Mol. Struc.*, 1985, 132:1–476; *J. Mol. Struct.* 1986, 155:1–402; *J. Mol. Struct.* 1987, 171:1–359; *J. Mol. Struct.*, 1988, 191:1–342; *J. Mol. Struct.*, 1989, 215:1–386.

which results in overdeconvolution (i.e., the half-bandwidth is overestimated and side lobes appear in the spectrum) or underdeconvolution (i.e., the half-bandwidth is underestimated and the deconvolved spectrum is smoothed). The optimum γ for deconvolution can be determined from several deconvolutions where γ is varied while both K and $D_g(x)$ are held constant (Fig. 13). Figure 13A clearly shows that the deconvolved spectrum using $\gamma = 5$ cm^{-1} is heavily smoothed (i.e., underestimation of γ); the peaks maintain a high degree of Lorentzian character and there is *decreased resolution* compared to the measured IR spectrum. The deconvolved spectrum shown in Fig. 13C using $\gamma = 15$ cm^{-1} reveals negative side lobes in the region of the $\bar{\nu}_s$ CH_2 band (near 2850 cm^{-1}), which indicates overestimation of the half-bandwidth value. Side lobes make spectral interpretation difficult and should be avoided when deconvolving IR spectral lines.

In addition to HWHH and K, an apodization function used for smoothing the deconvolved spectrum is chosen during the Fourier deconvolution of IR spectra. In contrast to the actual measurement of condensed phase spectra, where the particular apodization function does not significantly affect the final spectrum, the particular apodization function used for deconvolution greatly affects the signal-to-noise in the deconvolved spectrum. The dependence of (S/N)′ on $D_g(x)$ is illustrated in Fig. 14 for the C–H stretching region of diC_{12}PC bilayers. Using $K = 2.7$ and the six different apodization functions that are included with the Nicolet DECON deconvolution program, these deconvolved spectra show significant differences in (S/N)′ depending on the particular $D_g(x)$ used. The noise is no longer random, and peaks and valleys in the deconvolved spectrum are periodic, with a period of $1/L$ cm^{-1}. At this high K value it is evident that the Bessel function (Fig. 14C) and the cosine function (Fig. 14D) provide the highest (S/N)′ relative to the other apodization functions.

Fourier deconvolution has its greatest utility when spectral information can be obtained only through the use of this resolution enhancement technique. This is illustrated by the C=O stretching bands in the region of 1750–1700 cm^{-1} for the interfacial carbonyl esters of completely hydrated dilauroylphosphatidylcholine (diC_{12}PC) bilayer (22) (Fig. 15A) and an "anhydrous" diC_{12}PC lipid film (19) (Fig. 15B). The hydrated lipid bilayer spectrum shows a broad band with a peak position at 1731 cm^{-1}, whereas the lipid film has a narrower band with a peak position shifted to a higher wavenumber, 1738 cm^{-1}. The difference in the $\bar{\nu}$ C=O band positions are from (i) different conformations in the carbonyl ester groups due to a rotation about the C_1–C_2 bond of the glycerobackbone (23,24) and (ii) the fact that the carbonyl ester linked to the sn-2 glycerocarbon atom is hydrogen bonded to water, whereas the carbonyl ester linked to the sn-1 glycerocarbon atom is not (24). The sn-1 $\bar{\nu}$ C=O band typically occurs near 1741 cm^{-1}, whereas the sn-2 $\bar{\nu}$ C=O band position depends on the extent of phospholipid hydration. When phospholipids are completely dehydrated, the sn-2 $\bar{\nu}$ C=O band is near 1736 cm^{-1} (24), whereas for hydrated phospholipids it is near 1725 cm^{-1} (23,24). In Fig. 15, the deconvolved spectrum above each measured spectrum demonstrates that the broad carbonyl ester band is composed of two broad bands centered at 1740 and 1725 cm^{-1}, which correspond to the sn-1 C=O and the sn-2 C=O stretch, respectively. For aqueous suspensions of liposomes, the sn-2 carbonyl ester is completely hydrated as indicated by the high intensity of the 1725-cm^{-1} sn-1 $\bar{\nu}$ C=O band. In contrast, "anhydrous" lipid films (containing several molecules of hydration water) have a low-intensity shoulder at 1725 cm^{-1}, indicating that sn-2 C=O groups are dehydrated (Fig. 15). Several other applications of infrared spectroscopy applied to pharmaceutical problems are summarized in Table I.

ACKNOWLEDGMENT

Dr. C. Pidgeon was supported in part by NSF CTS 8908450 during the preparation of this paper.

REFERENCES

1. W. F. Maddams. The scope and limitations of curve fitting. *Appl. Spectrosc.* 34:245–267 (1980).
2. H. H. Mantsch, D. J. Moffatt, and H. L. Casal. Fourier transform methods for spectral resolution enhancement. *J. Mol. Struct.* 173:285–298 (1988).
3. J. K. Kauppinen, D. J. Moffatt, H. H. Mantsch, and D. G. Cameron. Fourier self-deconvolution: A method for resolving intrinsically overlapped bands. *Appl. Spectrosc.* 35:271–276 (1981).
4. J. K. Kauppinen. Fourier self-deconvolution in spectroscopy. In G. A. Vanasse (ed.), *Spectrometric Techniques, Vol. III,* Academic Press, New York, 1983, pp. 199–232.
5. P. R. Griffiths and G. L. Pariente. Introduction to spectral deconvolution. *Trends Anal. Chem.* 5:209–215 (1986).
6. H. H. Mantsch, H. L. Casal, and R. N. Jones. Resolution enhancement of infrared spectra of biological systems. In R. J. H. Clark and R. E. Hester (eds.), *Spectroscopy of Biological Systems, Advances in Spectroscopy, Vol. 13,* Wiley and Sons, New York, 1986, pp. 1–46.
7. J. K. Kauppinen, D. J. Moffatt, H. H. Mantsch, and D. G. Cameron. Fourier transforms in the computation of self-deconvoluted and first-order derivative spectra of overlapped band contours. *Anal. Chem.* 53:1454–1457 (1981).
8. J. K. Kauppinen, D. J. Moffatt, D. G. Cameron, and H. H. Mantsch. Noise in Fourier self-deconvolution. *Appl. Optics* 20:1866–1879 (1981).
9. W. Yang and P. R. Griffiths. Optimization of parameters for self-deconvolution: Minimization of noise and side-lobes without apodization. *Comput. Enhanced Spectrosc.* 1:157–165 (1983).
10. D. I. James, W. F. Maddams, and P. B. Tooke. The use of Fourier deconvolution in infrared spectroscopy. I. Studies with synthetic single-peak systems. *Appl. Spectrosc.* 41:1362–1370 (1987).
11. P. R. Griffiths and J. A. de Haseth. Fourier transform infrared spectrometry. In *Chemical Analysis, Vol. 83,* Wiley and Sons, New York, 1986.
12. A. A. Michelson. *Philos. Mag.* 31:256 (1891).
13. A. A. Michelson. *Philos. Mag.* 34:28 (1892).
14. G. Horlick. Introduction to Fourier transform spectroscopy. *Appl. Spectrosc.* 22:617–626 (1968).
15. R. N. Bracewell. Numerical transforms. *Science* 248:697–704 (1990).
16. P. C. Gillette and J. C. Koenig. Objective criteria for absorbance subtraction. *Appl. Spectrosc.* 38:334–337 (1984).
17. J. R. Powell, F. M. Wasacz, and R. T. Jakobsen. An algorithm for the reproducible spectral subtraction of water from the FT-IR spectra of proteins in dilute solutions and adsorbed monolayers. *Appl. Spectrosc.* 40:339–344 (1986).
18. P. R. Griffiths, J. A. de Haseth, and L. V. Azarraga. Capillary GC/FTIR. *Anal. Chem.* 55:1361A–1387A (1988).
19. C. Pidgeon, G. Apostol, and R. Markovich. Fourier transform infrared assay of liposomal lipids. *Anal. Biochem.* 181:28–32 (1989).
20. R. N. Jones, R. Venkataraghavan, and J. W. Hopkins. The control of errors in infrared spectrophotometry. I. The reduction of finite spectral slit distortion by the method of "pseudo-deconvolution." *Spectrochim. Acta* 23A:925–939 (1967).
21. R. N. Bracewell. *The Fourier Transform and Its Applications,* 2nd ed., McGraw–Hill, New York, 1978.
22. C. Pidgeon and R. J. Markovich. Formation of the antiplanar-antiplanar phosphate conformation of dilauroylphosphatidylcholine bilayers. *Biochim. Biophys. Acta* 1029:173–184 (1990).
23. H. L. Casal and H. H. Mantsch. Polymorphic phase behavior of phospholipid membranes studied by infrared spectroscopy. *Biochim. Biophys. Acta* 779:381–401 (1984).
24. P. T. T. Wong and H. H. Mantsch. High-pressure infrared spectroscopic evidence of water binding sites in 1,2-diacyl phospholipids. *Chem. Phys. Lipids* 46:213–224 (1988).
25. E. M. Suzuki and W. R. Gresham. Forensic science applications of diffuse reflectance infrared Fourier transform spectroscopy (DRIFTS). I. Principles, sampling methods, and advantages. *J. Forens. Sci.* 31:931–952 (1986).
26. E. M. Suzuki and W. R. Gresham. Forensic science applications of diffuse reflectance infrared Fourier transform spectroscopy (DRIFTS). II. Direct analysis of some tablets, capsule powders, and powders. *J. Forens. Sci.* 31:1292–1313 (1986).
27. P. R. Griffiths and M. P. Fuller. Mid-infrared spectrometry of powdered samples. *Adv. Infrared Raman Spectrosc.* 9:63–129 (1982).
28. R. J. Markovich. *Fourier Transform Infrared Studies of Immobilized and Mobilized Artificial Membranes,* Ph.D. dissertation, Purdue University, West Lafayette, Ind., 1990.
29. R. J. Markovich, J. M. Stevens, and C. Pidgeon. Fourier transform infrared assay of membrane lipids immobilized to silica: Leaching and stability of immobilized artificial membrane-bonded phases. *Anal. Biochem.* 182:237–244 (1989).
30. J. M. Stevens, R. J. Markovich, and C. Pidgeon. Characterization of immobilized artificial membrane HPLC columns using deoxynucleotides as model compounds. *Biochromatography* 4:192–205 (1989).
31. R. N. A. H. Lewis and R. N. McElhaney. Subgel phases of n-saturated diacylphosphatidylcholines: A Fourier transform infrared spectroscopic study. *Biochemistry* 29:7936–7953 (1990).
32. D. M. Byler and H. Susi. Examination of the secondary structure of proteins by deconvolved FTIR spectra. *Biopolymers* 25:469–487 (1986).
33. W. K. Surewicz and H. H. Mantsch. New insight into protein secondary structure from resolution-enhanced infrared spectra. *Biochim. Biophys. Acta* 952:115–130 (1988).
34. M. Jackson, P. I. Haris, and D. Chapman. Fourier transform infrared spectroscopic studies of lipids, polypeptides and proteins. *J. Mol. Struct.* 214:329–355 (1989).
35. K. Knutson, R. O. Potts, D. B. Guzek, G. M. Golden, J. E. McKie, W. J. Lambert, and W. I. Higuchi. Macro- and molecular physical-chemical considerations in understanding drug transport in the stratum corneum. *J. Control. Release* 2:67–87 (1985).
36. T. Kai, V. H. W. Mak, R. O. Potts, and R. H. Guy. Mechanism of percutaneous penetration enhancement: Effect of n-alkanols on the permeability barrier of hairless mouse skin. *J. Control. Release* 12:103–112 (1990).
37. V. H. W. Mak, R. O. Potts, and R. H. Guy. Percutaneous penetration enhancement in vivo measured by attenuated total reflectance infrared spectroscopy. *Pharm. Res.* 7:835–841 (1990).